RESEARCH ARTICLE

Check for updates

In situ formation of nickel sulfide quantum dots embedded into a two-dimensional metal–organic framework for water splitting†

Jin Lin,[a,b] Huajun Zhou,[a,b] R. S. Amin,[c] Amani E. Fetohi,[c] K. M. El-Khatib, [c] Chao Wang,*[a,b] Li Guo*[b] and Yanzhong Wang [*a,b]

The synergistic interaction between metal–organic frameworks (MOFs) and transition metal sulfides (TMS) has been a research hotspot in the field of electrocatalytic water splitting. Herein, nickel sulfide quantum dots@NiFe-terephthalic acid nanosheet (NSQDs@NiFe-TPA) composites were prepared by a two-step hydrothermal method. The size and crystal structure of nickel sulfides were easily modulated by adjusting the concentration of the sulfurizing agent. The *in situ* formed NiS/Ni_3S_2 quantum dots with grain sizes of around 5 nm were evenly dispersed on the surface of NiFe-TPA nanosheets, and the overpotential was only 219 mV at 10 mA cm^{-2}, and 90% current density could be maintained at 1.5 V (*vs.* RHE) for 60 h. When the concentration of the sulfurizing agent was increased up to 0.15 mmol L^{-1}, the as-prepared Ni_3S_2@NiFe-TPA exhibited an excellent HER performance. The overpotential is only 109 mV to reach a current density of 10 mA cm^{-2}, and it was attenuated by 20 mV after a 60 h stability test at a current density of 20 mA cm^{-2}. Furthermore, the overall water-splitting electrolyzer assembled with NSQDs@NiFe-TPA and Ni_3S_2@NiFe-TPA as anodic and cathodic electrodes exhibited a low cell voltage of 1.66 V at a current density 10 mA cm^{-2}, and almost no attenuation was observed after a 60 h stability test. The outstanding electrocatalytic properties of the as-prepared catalyst are due to the synergy of nickel sulfides and 2D MOFs that offers abundant accessible active sites, rapid ion/electron transportation, and convenient O_2/H_2 release channels.

1 Introduction

Due to the international economy's rapid growth, the demand for energy is growing. However, with the gradual depletion of traditional fossil energy and the resulting serious environmental pollution, it is urgent to develop sustainable clean energy sources.[1–3] Hydrogen (H$_2$), as a renewable, high-energy-density environment-friendly combustible gas, is an ideal energy source for replacing traditional fossil fuels.[4–7] Electrochemical water splitting is currently regarded as a practical way to produce hydrogen, but the process of redox reaction is kinetically sluggish due to its 4e$^-$ transfer and slow mass transfer process.[8] Therefore, an efficient electrocatalyst is crucial to reduce the potential of water splitting and thus save energy. Although noble-metal electrocatalysts such as ruthenium dioxide (RuO$_2$), iridium dioxide (IrO$_2$), and platinum carbon (Pt/C) exhibit an excellent catalytic performance, their industrial application is limited due to their high price and scarcity.[9] Therefore, the development of low-cost electrocatalysts has become a research hotspot in this field.[10]

Due to their extremely high specific active area, abundance of metal active sites, and adaptable structure and composition, metal–organic frameworks (MOFs), porous crystalline materials consisting of metal ions (clusters) and organic ligands, have drawn significant interest as prospective electrocatalysts.[11,12] Unfortunately, the relatively low electronic conductivity and poor stability of most MOFs limit their application as an efficient electrocatalyst. In order to evade the issues, MOFs are generally employed as precursors for preparing porous metal compounds (oxides, selenides, sulfides and phosphides) *via* pyrolysis or chemical treatment. However, the porous and ordered structure of MOFs is inevitably destroyed, resulting in the reduction of active sites. Due to these issues, optimizing the structures of MOFs is considered as a practical strategy to enhance their catalytic performance. For instance,

[a]School of Materials Science and Engineering, North University of China, Taiyuan 030051, P. R. China. E-mail: wangchao_nuc@126.com, wyzletter@nuc.edu.cn
[b]Institute of Advanced Energy Materials and System, North University of China, Taiyuan 030051, P. R. China. E-mail: gl814@qq.com
[c]Chemical Engineering Department, Engineering Research and Renewable Energy Institute, National Research Centre, 33 El-Buhouth St., Dokki, Cairo, 12622, Egypt
†Electronic supplementary information (ESI) available. See DOI: https://doi.org/10.1039/d2qi02279f

1294 | *Inorg. Chem. Front.*, 2023, **10**, 1294–1304

This journal is © the Partner Organisations 2023

Xing *et al.* prepared a 2D Co-MOF using HITP (2,3,6,7,10,11-hexaiminotriphenylene) as the coordination system, and the intrinsic conductivity of the catalyst was improved by optimizing the π-D conjugation between the ligand and metal ions, thus enhancing the oxygen release capacity.[13] Another promising method is to improve the electrocatalytic performance of MOFs composited with conductive materials,[14] such as metal,[15] metal oxides/sulfides/phosphides/selenides,[16–18] and conductive carbon nanomaterials.[19,20] Among various metal compounds, transition metal sulfides (TMS) including nickel sulfide, molybdenum sulfide and tungsten sulfide have amazing potential in electrocatalytic water splitting owing to their high electronic conductivity, and inexpensive and easy manufacturing process.[21,22] Therefore, transition metal sulfides are widely used as a promising second phase integrated with MOFs to effectively enhance their electronic conductivity, thus resulting in boosting the electrocatalytic performance of MOFs.[23] For instance, Muhammad Fiaz *et al.* introduced transition metal sulfides as a conductive agent to intensify the electronic conductivity of MOFs, greatly improving the OER activity of MOFs.[24] However, the step-by-step preparation of metal sulfides/MOF composites results in an uneven distribution of metal sulfides and MOFs, which inhibits the transfer of electrons and ions at the interface between metal sulfides and MOFs. To address this issue, the *in situ* formation of metal sulfides derived from MOFs was proposed to synthesize transition metal sulfide@MOF hybrid electrocatalysts *via* a controlled vulcanization. He *et al.* prepared a layered structure NiS/Ni-MOF hybrid electrocatalyst by the partial vulcanization of Ni-MOF nanosheets *via* a hydrothermal method.[25] Herein, in the NiS/Ni-MOF electrocatalyst the porous structure of the MOF was retained, and meanwhile the *in situ* formed metal sulfide could intensify the electronic conductivity and structural stability of the MOF. However, the as-formed metal sulfides cover the surface of MOFs, which can inhibit the exposure of MOF active sites. Furthermore, vulcanization still inevitably destroys the porous structure of MOFs. To circumvent the above problems, the optimization of the size and structure of the *in situ* formed metal sulfides is an effective method. In general, when the size of the catalyst attains a nanoscale structure, the electron transfer pathway can be effectively reduced, and the edge active site can be fully exposed to improve the activity of the catalyst.[26] Nurlaela *et al.* revealed that the performance of an electrocatalyst is inversely proportional to its size.[27] Therefore, designing electrocatalysts smaller than 5 nm is crucial for improving the structure and functionality of electrocatalysis. Chen *et al.* prepared Mo-Ni_3S_2 quantum dots (QDs) with uniformly dispersed and S-rich defects by a simple two-step hydrothermal method.[28] A large number of S-defects provide an electrochemically active surface area (ECSA) with abundant electrocatalytically active sites and rapid electron transport, which results in the low overpotentials of the HER and OER of 115 and 222 mV at 10 mA cm^{-2}, respectively. However, because of their high surface energy, QDs have a propensity to aggregate throughout the catalytic process.[29] Therefore, developing an effective

method to prevent the agglomeration of QDs is one of the keys to optimize their electrocatalytic performance. As we know, the *in situ* formation of metal sulfide QDs derived from 2D MOFs have been rarely reported. The *in situ* formation of metal sulfide QDs not only exposes more electrocatalytic sites, but also optimizes the electrical conductivity of MOFs. Furthermore, it will also avoid damaging the porous and ordered structure of MOFs, which can ensure that the active sites of MOFs can participate in electrocatalytic reactions.

Herein, we prepared nickel sulfide QDs@NiFe-TPA composite electrocatalysts by a simple two-step hydrothermal process. The grain size, crystal structure and electronic structure of nickel sulfides and MOFs can be easily adjusted by regulating the concentration of the sulfurizing agent. Nickel sulfide QDs were formed *in situ* with a 0.075 mmol L^{-1} vulcanizing agent and uniformly dispersed onto the surface of NiFe-TPA nanosheets (denoted as NSQDs@NiFe-TPA), which exhibited remarkable electrocatalytic properties for the OER in alkaline media, with a low overpotential of 219 mV at 10 mA cm^{-2}. In addition, the assembled electrolyzers with NSQDs@NiFe-TPA and Ni_3S_2@NiFe-TPA as anode and cathode electrodes required 1.66 V to achieve a current density of 10 mA cm^{-2} along with excellent durability.

2 Experiment

2.1 Materials

Nickel chloride hexahydrate ($NiCl_3·6H_2O$), ferrous chloride hexahydrate ($FeCl_2·6H_2O$), terephthalic acid (TPA), thioacetamide (TAA), *N,N*-dimethylformamide (DMF), absolute ethanol, and potassium hydroxide were purchased from Shanghai Aladdin Biochemical Technology and were not purified.

2.2 Synthesis of NiFe-TPA

Nickel foam (NF) (2 cm × 3 cm) was ultrasonically cleaned for 15 min with HCl (3 M), deionized water and ethanol, respectively, and then dried in a vacuum oven at 60 °C for 6 h. $FeCl_2·6H_2O$ (18.64 mg), $NiCl_3·6H_2O$ (66.85 mg) and TPA (62.3 mg) were dissolved in 16 mL of DMF containing 1 mL of absolute ethanol and 1 mL of deionized water, and stirred evenly for 30 min. Then, the cleaned NF was transferred into the mixed solution in a Teflon-lined stainless autoclave (50 mL) at 120 °C and autoclaved for 12 h. The resulting samples were washed using ultrasound with deionized water and ethanol three times and dried under vacuum at 60 °C for 6 h, and have been denoted as NiFe-TPA.

2.3 Synthesis of NSQDs@NiFe-TPA

0.075 mmol L^{-1} TAA was added to 25 mL absolute ethanol and stirred evenly for 30 min, then the solution was transferred to a 30 mL reaction kettle, and the NiFe-TPA/NF was vertically placed over the mixed solution in a Teflon-lined stainless autoclave at 150 °C and autoclaved for 9 h. The samples were washed using ultrasound with deionized water and ethanol, and was then dried at 60 °C for 6 h in a vacuum oven.

This journal is © the Partner Organisations 2023

Inorg. Chem. Front., 2023, **10**, 1294–1304 | **1295**

2.4 Synthesis of Ni₃S₂@NiFe-TPA

The synthesis method was the same as that of NSQDs@NiFe-TPA except that the TAA concentration was 0.15 mmol L^{-1}.

2.5 Preparation of RuO₂ and Pt/C electrodes

The catalyst ink was prepared by pouring 10 mg of RuO₂ (Pt/C) into a mixture of 985 μL ethanol and 15 μL 10 wt% Nafion solution and sonicating for 30 min. 250 μL of the catalyst ink was evenly coated on a surface of 1 cm^2 of the nickel foam, and was dried under vacuum for 6 h. The catalyst loading was about 2.5 mg cm^{-2}.

2.6 Characterization

Scanning electron microscopy (SEM, JEOL JSM-7001F) and transmission electron microscopy (TEM, JEOL JEM 2100F) were used to detect the morphology of the samples. Fourier transform infrared spectroscopy (FTIR) was performed on a Bruker Vertex 70 spectrometer. X-ray photoelectron spectroscopy (XPS) was performed on an XPS-7000 spectrometer (Rigaku) using Mg Kα radiation. Crystal structures of the materials were probed using an X-ray diffractometer (XRD, Bruker D8 ADVANCE Germany, Cu Kα radiation).

2.7 Electrochemical measurements

All electrochemical tests were carried out on an electrochemical workstation (Bio-logic, SP-200, France) using a three-electrode system. The experimental tests were carried out using a three-electrode system with 1M KOH electrolyte solution. An electrocatalyst electrode with an area of 1 cm^2 was used as the working electrode, a platinum sheet was used as the auxiliary electrode, and an Ag/AgCl electrode was used as the reference electrode. The Nernst equation was used for all potential transformations:[30]

$$E_{\mathrm{RHE}} = E + 0.059 \times \mathrm{pH} + E_{\mathrm{Ag/AgCl}} \tag{1}$$

The overpotentials were calculated using the following equations:[30]

$$\eta_{\mathrm{OER}} = E_{\mathrm{RHE}} - 1.23\ \mathrm{V} \tag{2}$$

$$\eta_{\mathrm{HER}} = E_{\mathrm{RHE}} - 0\ \mathrm{V} \tag{3}$$

All curves were not compensated by the IR potential.
The Tafel equation:

$$\eta = b \log j + a \tag{4}$$

where the overpotential, Tafel slope, current density, and potential at 1 mA cm^{-2} are represented by η, b, j and a, respectively.

Linear sweep voltammetry (LSV) was tested with a scanning speed of 5 mV s^{-1}. Electrochemical impedance spectroscopy (EIS) was performed at frequencies ranging from 10^5 to 0.01 Hz, and a bias of 250 and 200 mV was applied during the OER and HER tests, respectively. Electrochemically active surface area (ECSA) was evaluated from non-Faraday capacitance measurements. The electrochemical double layer capacitance (C_{dl}) could be measured by cyclic voltammetry (CV) in the range of 0.42 to 0.62 V (*vs.* RHE) with the scan rates being 10, 20, 30, 40 and 50 mV s^{-1}. Finally, C_{dl} obtained from the linear slope represented the ECSA.

3 Results and discussion

3.1 Morphologies and structures of samples

The synthesis process of electrocatalysts is shown in Fig. 1(a). First, 2D NiFe-TPA nanosheets were *in situ* grown on the NF backbone by a simple hydrothermal method. Then, the as-prepared NiFe-TPA/NF was vulcanized with different concentrations of TAA, resulting in the *in situ* formation of nickel sulfides with different grain sizes and crystal phases on the surface of NiFe-TPA naosheets. The morphology and composition of catalysts were characterized by SEM and TEM. As shown in Fig. 1b, NiFe-TPA exhibits a sheet-like structure and uniformly grew on NF backbones. After the vulcanization with 0.075 mmol L^{-1} TAA, the sheet-like structure of NiFe-TPA still remained well without significant changes (Fig. 1c). When the concentration of TAA was increased up to 0.15 mmol L^{-1}, many nanoparticles with a diameter of about 50–100 nm appeared and uniformly dispersed on the surface of NiFe-TPA nanosheets (Fig. 1d). The morphologies of NSQDs@NiFe-TPA and Ni₃S₂@NiFe-TPA were further investigated by TEM. As shown in Fig. 1e and f, many quantum dots with a diameter of about 5 nm are observed, and they are uniformly embedded on the surface of NiFe-TPA nanosheets. The HRTEM image of NSQDs@NiFe-TPA reveals that the lattice spacings are 0.276 and 0.204 nm, which correspond to the crystal planes (300) of NiS and (202) of Ni₃S₂, respectively. In contrast, Fig. S1a† shows that many nanoparticles with a grain size of 50–100 nm are uniformly dispersed on the surface of MOF nanosheets, and the HRTEM image reveals that the lattice spacings are 0.408 and 0.204 nm, which correspond to the crystal planes (101) and (202) of Ni₃S₂, respectively (Fig. S1b†). As we know, TAA decomposed into S^{2-} at a high temperature is easy to combine with metal ions of MOFs to form metal sulfides. However, when the concentration of TAA is low and not enough to disintegrate the structure of MOFs, the growth of metal sulfide crystal nuclei is limited under the action of the organic ligand TPA and thus *in situ* formed nickel sulfide quantum dots are embedded on MOF nanosheets without destroying their structures. However, on increasing the concentration of TAA, the metal sulfide crystals grow up gradually until the restriction effect of organic ligands can be neglected, which results in the loading of metal sulfide nanoparticles on the surface of MOFs. This unique 0D/2D structure is conducive to provide abundant active sites for electrochemical reactions and accelerate mass transfer. The EDX mapping results (Fig. 1g) showed that C, O, Ni, Fe and S were uniformly distributed on NSQDs@NiFe-TPA, indicating that the metal sulfide was dispersed evenly on the surface of MOFs, which was conducive to the exposure of the active sites.
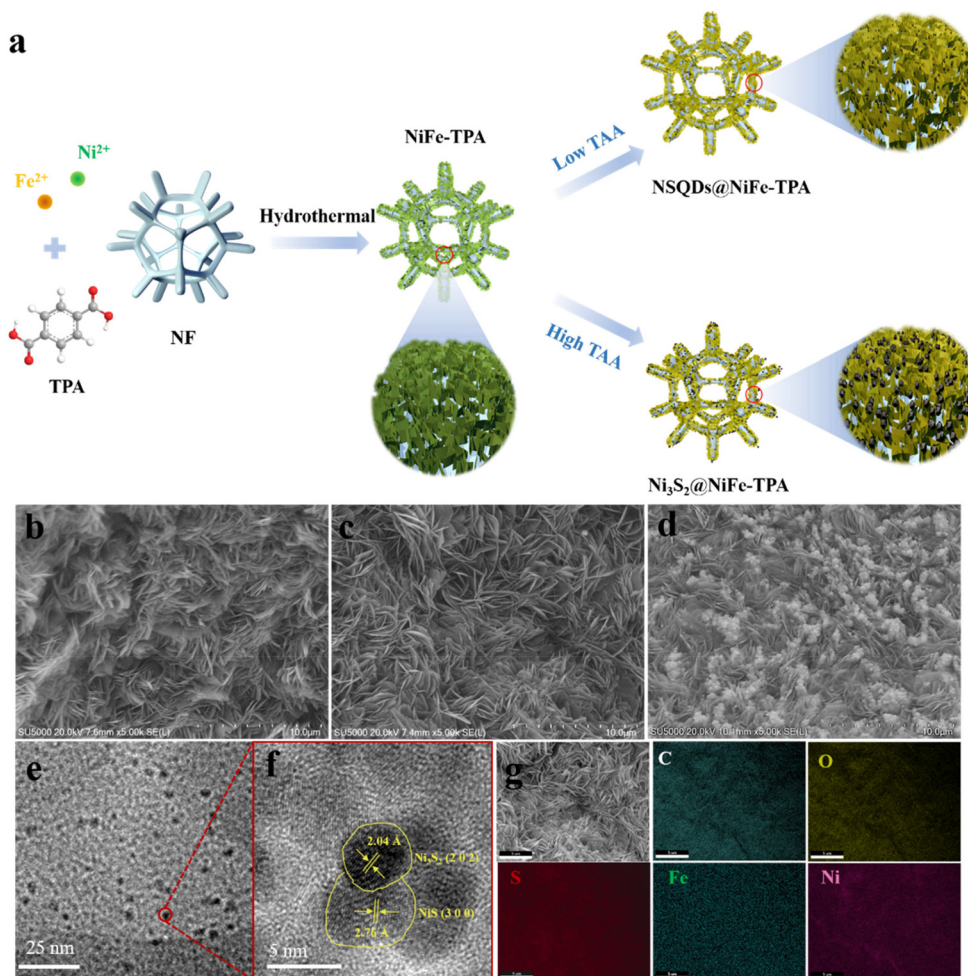
1296 | *Inorg. Chem. Front.*, 2023, **10**, 1294–1304

This journal is © the Partner Organisations 2023

Fig. 1 (a) Schematic diagram of the synthesis process of NiFe-TPA, NSQDs@NiFe-TPA and Ni$_3$S$_2$@NiFe-TPA. SEM images of (b) NiFe-TPA, (c) NSQDs@NiFe-TPA and (d) Ni$_3$S$_2$@NiFe-TPA, (e and f) HRTEM images of NSQDs@NiFe-TPA, and (g) EDX mapping of NSQDs@NiFe-TPA.

In order to further determine the structure and composition of the catalysts, the crystal structures of the samples were examined by XRD. As shown in Fig. 2a, NSQDs@NiFe-TPA exhibits strong diffraction peaks located at 8.8°, 15.9° and

17.9°, which are consistent with the XRD patterns of NiFe-TPA.[31] It indicates that the NiFe-MOF phase still remains after the vulcanization with 0.075 mmol L^{-1} TAA. Nevertheless, weak peaks located at 30.3, 32.2 and 38.8° correspond to the
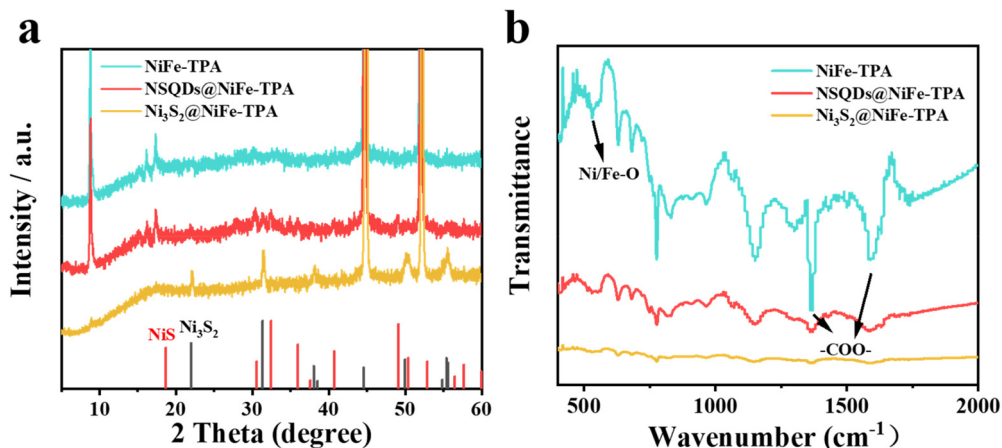

Fig. 2 (a) XRD patterns and (b) FT-IR spectra of NiFe-TPA, NSQDs@NiFe-TPA and Ni$_3$S$_2$@NiFe-TPA.

(101), (300) and (131) crystal planes of NiS, respectively, and the peaks located at 21.7, 31.04 and 44.3° correspond to the (101), (110) and (202) crystal phases of Ni_3S_2, which is consistent with the results of TEM.[32] However, the characteristic diffraction peaks of NiFe-TPA and NiS become very weak after the vulcanization with 0.15 mmol L^{-1} TAA, and the peaks located at 21.7, 31.04, 44.3, 49.7 and 55.1° correspond to the (101), (110), (202), (113) and (122) crystal planes of Ni_3S_2.[33] It suggests that metal sulfides gradually transformed from thermodynamically unstable NiS to stable Ni_3S_2 on increasing the concentration of TAA.[34,35] Moreover, no characteristic peaks of iron sulfide were observed after the vulcanization. It is attributed to the fact that the solubility of nickel sulfide ($K_{sp\ (NiSx)}$) is smaller than that of iron sulfide ($K_{sp\ (FeSx)}$), implying that Ni ions in NiFe -TPA are more likely to form nickel sulfide and precipitate compared with Fe during the vulcanization.[36] To evaluate the surface functional group of the prepared samples, Fourier transform infrared spectroscopy (FT-IR) was performed. Fig. 2b shows that NSQD@NiFe-TPA exhibits similar FT-IR spectra compared to NiFe-TPA. The peaks centered at around 1581 and 1386 cm^{-1} correspond to the coordination modes of V_{as} (–COO–) and V_s (–COO–) between metal centers and organic linkers, respectively,[37] indicating the presence of carboxylic acid groups exposed on the surface of NiFe-TPA, which is favorable for the adsorption of H_2O for NSQDs@NiFe-TPA during the water splitting process. The peak located at 540 cm^{-1} is associated with the coordination bond vibration between the metal atom (Ni/Fe) and the carboxyl group, indicating the presence of a metal–oxygen (M–O) bond in NiFe-TPA and NSQDs@NiFe-TPA. In addition, the intensity of peaks decreased with the increase of the vulcanization degree, indicating that metal ions in MOFs were

constantly precipitated during the vulcanization, leading to a gradual disintegration of MOFs.[37] Although MOFs were gradually decomposed during the vulcanization, the characteristic peaks of the ligand were still retained, indicating that NiFe-TPA could still maintain its structure and form a heterogeneous catalyst with nickel sulfides, which is consistent with the results of XRD and TEM. However, the characteristic peaks of metal–oxygen and the ligand disappeared with a high TAA concentration (0.15 mmol L^{-1}), suggesting the complete decomposition of NiFe-TPA and resulting in the *in situ* formation of Ni_3S_2.

To further investigate the chemical composition and valence state of electrocatalysts, X-ray photoelectron spectra (XPS) of NiFe-TPA and NSQDs@NiFe-TPA were recorded and are shown in Fig. 3. As shown in Fig. 3a, the survey spectra of XPS show the co-presences of C, O, S, Fe and Ni elements in NSQDs@NiFe-TPA, which is consistent with the results of EDX. Fig. 3b shows that the high-resolution C 1s spectrum of NSQDs@NiFe-TPA is similar to that of NiFe-TPA without any significant changes, and indicates the presence of C–C, C–O and C=O bonds.[38] The same result can also be verified in the high-resolution O 1s spectrum (Fig. 3c). After vulcanization, the strength of the Ni/Fe–O bond decreased significantly, while the peak intensities of –O–C=O and –OH did not change, indicating that the formation of NSQDs would not lead to the large-scale decomposition of MOFs.[39] As shown in Fig. 3d, the high-resolution Ni 2p spectra of NSQDs@NiFe-TPA shows typical peaks centered at 873.98 and 856.21 eV, which are attributed to Ni $2p_{1/2}$ and Ni $2p_{3/2}$, respectively.[40] The peak centered at 852.9 eV corresponds to Ni^0 in the nickel foam, and the peak intensity of NSQDs@NiFe-TPA increases compared with NiFe-TPA, which may be attributed to the formation of the Ni–Ni bond in Ni_3S_2 after vulcanization.[41] Significantly,
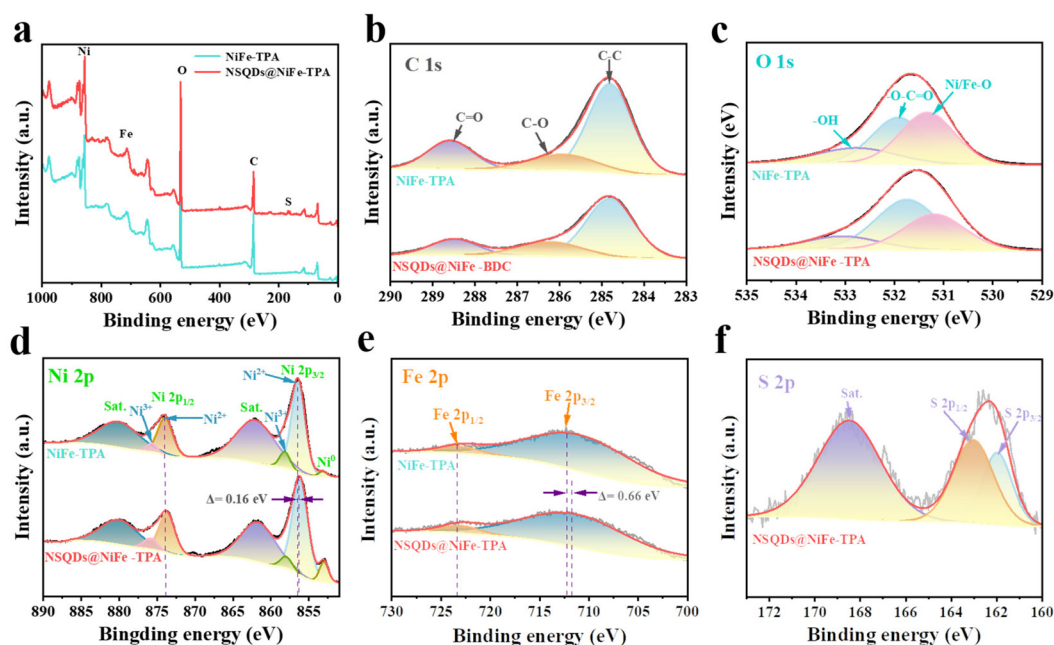

Fig. 3 (a) XPS survey spectra, high resolution XPS of (b) C 1s, (c) O 1s, (d) Ni 2p, (e) Fe 2p and (f) S 2p of NiFe-TPA and NSQDs@NiFe-TPA.

1298 | *Inorg. Chem. Front.*, 2023, **10**, 1294–1304

This journal is © the Partner Organisations 2023

the binding energies of Ni $2p_{3/2}$ of NSQDs@NiFe-TPA were reduced by 0.16 eV in comparison with the pristine NiFe-TPA (856.37 eV). Meanwhile, the high-resolution Fe 2p spectrum shows a similar phenomenon. The binding energies of Fe $2p_{1/2}$ and Fe $2p_{3/2}$ of NSQDs@NiFe-TPA are 723.65 and 711.37 eV, respectively. Compared with pristine NiFe-TPA, the binding energy of Fe $2p_{3/2}$ of NSQDs@NiFe-TPA was reduced by 0.66 eV. It shows the interfacial interaction between NiFe-TPA and NSQDs, which is effective in shortening and speeding up the electron transfer pathway and rate during the catalytic process.[42] In addition, the peaks of S $2p_{1/2}$ and S $2p_{3/2}$ in high resolution S 2p spectrum (Fig. 3f) revealed the successful synthesis of NSQDs in NSQDs@NiFe-TPA.[26]

3.2 Electrocatalytic performance of OER

Linear sweep voltammetry (LSV) curves were recorded using a conventional three-electrode cell with 1.0 M KOH solution to assess the impact of vulcanization on the OER characteristics of NiFe-TPA. The comparison samples including NiFe-TPA, Ni_3S_2@NiFe-TPA, NF and RuO_2 were also tested under the same conditions. Cathode scans were used to record all LSV curves as backward curves in order to rule out any potential catalyst oxidation-related contributions to the catalytic current. Fig. 4a shows that NSQDs@NiFe-TPA exhibits the best OER performance, and it only requires a low overpotential of 219 mV to obtain a current density of 10 mA cm^{-2}, which is much lower than that of NiFe-TPA (248 mV), Ni_3S_2@NiFe-TPA (337 mV), RuO_2 (305 mV), and NF (420 mV). For comparison, the histogram of overpotentials at different current densities of 10, 50 and 100 mA cm^{-2} are shown in Fig. 4b. NSQDs@NiFe-TPA requires the low overpotentials of 304 and 379 mV to drive the current densities of 50 and 100 mA cm^{-2},

which greatly reduces the energy consumption during the oxygen process, demonstrating its promising application potential. Fig. 4c shows the relevant Tafel curves for each catalyst to evaluate the OER dynamics. NSQDs@NiFe-TPA still exhibits a favorable Tafel slope (59.2 dec mV^{-1}), which is much lower than that of NiFe-TPA (72.9 dec mV^{-1}), Ni_3S_2@NiFe-TPA (122.2 dec mV^{-1}) and RuO_2 (117.4 dec mV^{-1}), respectively. It suggests that NSQDs@NiFe-TPA has a faster OER kinetics and mass transfer rate than that of other catalysts. In addition, Nyquist plots (Fig. 4d) show that the charge-transfer resistance (R_{ct}) of NSQDs@NiFe-TPA is only 1.0 Ω, which is much lower than those of NiFe-TPA (1.6 Ω) and Ni_3S_2@NiFe-TPA (14.1 Ω), respectively. It is worth noting that the smallest charge-transfer resistance of NSQDs@NiFe-TPA is attributed to the fact that 0D NSQDs embedded on 2D nanosheets can accelerate the charge-transfer at the interface of metal sulfides and MOFs. As shown in Table S1,† compared with non-precious metal OER catalysts in recent years, NSQDs@NiFe-BDC shows the superior OER performance. Its stability was tested by chronoamperometry. Fig. 4e shows that NSQDs@NiFe-BDC maintains 90% of the current density at a potential of 1.5 V (vs. RHE) for 60 h.

NSQDs@NiFe-TPA exhibits such a significant improvement compared with pristine NiFe-TPA, which is attributed that the synergistic effect of the in situ formed nickel sulfides quantum dots and MOFs. After vulcanization with an appropriate concentration of the vulcanizing agent, NiS and Ni_3S_2 quantum dots were generated on the original 2D MOFs nanosheets, and MOFs still retained the original two-dimensional structure. In addition, the generated metal sulfides can induce an interface effect with MOFs to regulate the electronic structure of metal ions and increase the binding energy of Ni and Fe (verified by the above XPS analysis), which is more conducive to the OER
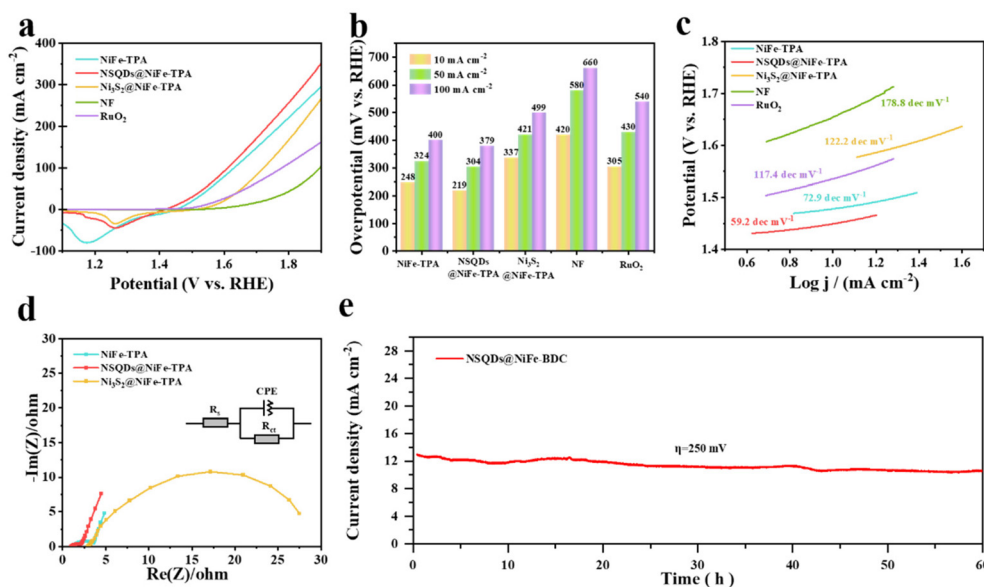

Fig. 4 (a) LSV curves, (b) comparison of the overpotential, (c) Tafel plots derived from LSV curves of NiFe-TPA, NSQDs@NiFe-TPA, Ni_3S_2@NiFe-TPA, NF and RuO_2, (d) Nyquist plots of NiFe-TPA, NSQDs@NiFe-TPA and Ni_3S_2@NiFe-TPA, (e) the chronoamperometry curve of NSQDs@NiFe-TPA at an overvpotential of 250 mV.

This journal is © the Partner Organisations 2023

Inorg. Chem. Front., 2023, **10**, 1294–1304 | **1299**

reaction.[43] In addition, the *in situ* formed nickel sulfides exists in the form of 0 D quantum dots, which have rich marginal active sites and large specific surface area, which provides the maximum contact with the electrolyte and enhances the electron transport during the catalytic process.[44] Therefore, NSQDs@NiFe-TPA greatly reduced the overpotential compared with pure NiFe-TPA. Unfortunately, the overpotential of Ni_3S_2@NiFe-TPA decreased compared with pure NiFe-TPA, which is attributed to the disintegration of NiFe-TPA by excessive vulcanization and thus the loss of active sites of MOFs. Furthermore, the generated Ni_3S_2 has slow kinetics due to its large particle size and poor adsorption of key intermediates (*OH, *OOH) in the catalytic process, resulting in large potentials to drive the reaction.[42]

To further investigate the evolution of the structure and composition of the catalyst in the OER process, the morphology, crystal structure and composition of NSQDs@NiFe-TPA were determined after the OER testing. As shown in Fig. S2,† the nanosheet structure of NSQDs@NiFe-BDC was still maintained well without a structural collapse, indicating an excellent structural stability. However, the XRD pattern (Fig. S3a†) shows that the characteristic peaks of NSQSs@NiFe-TPA completely disappear and a broad peak appears as shown in Fig. S3a,† indicating that NSQDs@NiFe-TPA was transformed into amorphous oxides/hydroxides during the process of the OER, which is the real catalytic active species for the OER.[45] The XPS of NSQDs@NiFe-TPA (Fig. S3b†) shows that the peak intensity of the C 1s spectrum decreases, especially for the C–O bond. The high-resolution O 1s spectrum (Fig. S3c†) show that the peak intensity of Ni/Fe–O increases significantly and the peak intensity of the –C═O bond of the carboxyl group decreases, indicating that MOFs decompose and *in situ* form hydroxides as the real active species during

OER, and this was also confirmed by the XRD results. Comparing the high-resolution Ni 2p and Fe 2p (Fig. S3d and e†) spectra after the OER test, the binding energy of the Ni 2p spectrum was reduced by 0.44 eV, and the binding energy of the Fe 2p spectrum was increased by 0.56 eV. This indicates that electrons are transferred from Fe to Ni in the MOFs, resulting in the high oxidation state of Fe ions and serving as the active sites of MOFs. Surprisingly, the Ni^{2+}/Ni^{3+} ratio decreased from 7.0 to 6.5, indicating a shift in the high oxidation phase of Ni throughout the catalytic system, indicating that nickel sulfides also serve as catalytic sites for the OER, which revealed the synergistic interaction between nickel sulfides and MOFs in NSQDs@NiFe-TPA.[46–51] Moreover, no peaks related to S 2p were observed after the OER test (Fig. S3f†), indicating that nickel sulfides were transformed into highly active Ni–OOH, which agrees with the results of XRD. It was further proved that NSQDs@NiFe-TPA is an excellent pre-catalyst for the OER.

3.3 Electrocatalytic performance of HER

The HER performance of samples was also measured in a three-electrode cell with 1 M KOH solution. As shown in Fig. 5a, a commercial Pt/C catalyst was employed as a benchmark for comparison. It can be seen that Ni_3S_2@NiFe-TPA exhibits the highest excellent HER activity with an overpotential of 109 mV at a current density of 10 mA cm^{-2}, which is superior to NiFe-TPA (193 mV) and NSQDs@NiFe-TPA (142 mV), but is inferior to commercial Pt/C (24 mV) (Fig. 5b). NiFe-TPA exhibits a similar HER activity with bare nickel foam, indicating the negligible HER catalytic property of NiFe-TPA due to its low active sites and poor electronic conductivity. Nevertheless, the *in situ* formed NiS and Ni_3S_2 with high electronic conductivities were loaded on MOFs, which accelerated
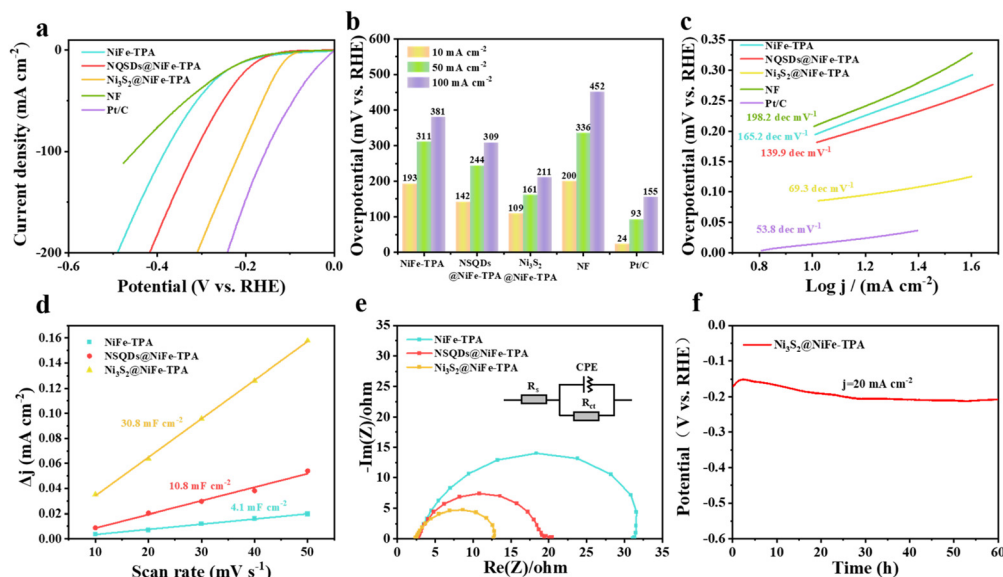

Fig. 5 (a) LSV curves, (b) comparison of the overpotentials, (c) Tafel plots derived from LSV curves, (d) double-layer capacitance (C_{dl}) plots of NiFe-TPA, NSQDs@NiFe-TPA, Ni_3S_2@NiFe-TPA, NF and Pt/C, (e) Nyquist plots of NiFe-TPA, NSQDs@NiFe-TPA and Ni_3S_2@NiFe-TPA, (f) chronopotentiometry (CP) curve of Ni_3S_2@NiFe-TPA at a current density of 20 mA cm^{-2}.
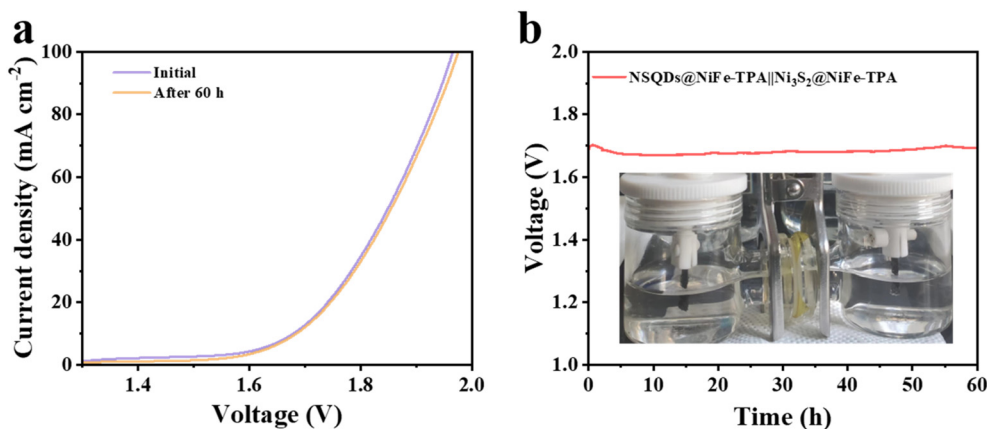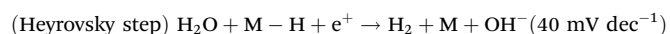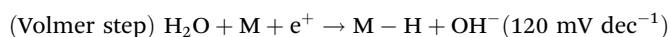
Fig. 6 (a) Comparison of LSV curves of NSQDs@NiFe-TPA ‖ Ni_3S_2@NiFe-TPA after 60 h of stability testing, (b) chronopotentiometry curve of NSQDs@NiFe-TPA ‖ Ni_3S_2@NiFe-TPA at a current density of 10 mA cm^{-2}.

the electron transfer rate between the carrier and served as active sites for HER, enhancing the HER activity of NSQDs@NiFe-TPA. However, after further vulcanization, the only phase of metal sulfides in the catalyst is Ni_3S_2. Compared with NiS, Ni_3S_2 has Ni–S bond as well as the Ni–Ni bond. The existence of the Ni–Ni bond in Ni_3S_2 results in a metal-like conductivity, thus boosting the electron transfer of the catalyst during the HER. In addition, a large amount of Ni ions in Ni_3S_2 is conducive to exposing more active sites and increasing the adsorption of the intermediate H*, thus accelerating the HER performance.[52,53] To further assess the intrinsic characteristics of catalysts, we analyzed the Tafel plots of the catalysts with different degrees of vulcanization (Fig. 5c). The Tafel slopes of NiFe-TPA, NSQDs@NiFe-TPA and Ni_3S_2@NiFe-TPA are shown in Fig. 5c. It is worth noting that the Tafel slope of Ni_3S_2@NiFe-TPA (69.3 dec mV^{-1}) is significantly lower than those of NSQDs@NiFe-TPA (139.9 dec mV^{-1}) and NiFe-TPA (165.2 dec mV^{-1}), indicating that NSQDs@NiFe-TPA follows a Volmer–Heyrovsky mechanism according to the reaction steps of the HER:[54]

$$\text{(Volmer step) } H_2O + M + e^+ \rightarrow M-H + OH^- \, (120 \text{ mV dec}^{-1})$$

$$\text{(Heyrovsky step) } H_2O + M-H + e^+ \rightarrow H_2 + M + OH^- \, (40 \text{ mV dec}^{-1})$$

To indicate the catalytic activity of all samples, the ECSA of the catalysts was determined by C_{dl} *via* CV at different sweep speeds in the voltage window of a non-Faraday region. As shown in Fig. 5d, Ni_3S_2@NiFe-TPA exhibits the largest double layer capacitance (30.8 mF cm^{-2}), which is much higher than those of NSQDs@NiFe-TPA (10.8 mF cm^{-2}) and NiFe-TPA (4.1 mF cm^{-2}). The reason is that Ni_3S_2 is the only sulfide with a high concentration of vulcanizing agent. Compared with NiS, Ni_3S_2 with more Ni sites is favorable for H* adsorption, resulting in a large electrochemically active surface area. Moreover, EIS analysis was carried out to investigate the kinetics of the HER for all samples. As shown in Fig. 5e, all samples exhibit a

small solution resistance (R_s = 2.5 Ω). In addition, the charge transfer resistance (R_{ct}) of Ni_3S_2@NiFe-TPA is 5.31 Ω, which is much lower than those of NSQDs@NiFe-TPA (8.32 Ω) and NiFe-TPA (14.41 Ω), respectively. Such a phenomenon may be attributed to the excellent electronic conductivity of Ni_3S_2. As shown in Table S2,† compared with non-precious metal HER catalysts, Ni_3S_2@NiFe-TPA shows an outstanding HER performance. To evaluate the potential application of Ni_3S_2@NiFe-TPA, the stability of Ni_3S_2@NiFe-TPA was tested by chronopotentiometry (CP). As shown in Fig. 5f, the overpotential was only attenuated by 20 mV after 60 h of stability testing. The SEM image (Fig. S4†) shows that Ni_3S_2@NiFe-TPA still maintained the 2D structure with many nanoparticles on the surface of nanosheets, and the XRD patterns (Fig. S5†) show that the peaks of Ni_3S_2 are still observed after the stability test of the HER, indicating the excellent stability during the HER.

3.4 Water splitting

Based on the outstanding OER and HER performances of NSQDs@NiFe-TPA and Ni_3S_2@NiFe-TPA, we believe that these two catalysts have great potential in the application of fully hydrolyzed water. Therefore, the two electrodes were assembled into an overall water splitting device, in which NSQDs@NiFe-TPA was used as the anode and Ni_3S_2@NiFe-TPA as the cathode. Fig. 6a shows that the hydrolysis device requires only a voltage of 1.66 V to achieve a current density of 10 mA cm^{-2}, and the device can work stably for 60 h without any significant voltage attenuation (Fig. 6b). Moreover, the LSV curve was almost unchanged after 60 h of the stabilization test, which further proves the potential application of the catalyst for water splitting.

4 Conclusions

NSQDs/NiFe-TPA and Ni_3S_2/NiFe-TPA have been successfully prepared by regulating the concentration of TAA by a two-step hydrothermal method, and they show an excellent catalytic

This journal is © the Partner Organisations 2023

Inorg. Chem. Front., 2023, **10**, 1294–1304 | **1301**

performance for the OER and HER, respectively. The assembled two-electrode configuration with NSQDs@NiFe-TPA and Ni_3S_2@NiFe-TPA as anode and cathode electrodes, respectively, was tested for overall water splitting in 1 M KOH. When the voltage was 1.66 V, the current density could reach 10 mA cm^{-2}, and the catalytic performance almost did not decay after 60 h of the stability test, exhibiting outstanding electrocatalytic activity and stability. The excellent eletrocatalytic properties are attributed to the optimized structure and electronic interaction between nickel sulfides and MOFs, resulting in exposing more eletrocatalytic sites and enhancing the electronic conductibility of MOFs. The self-supported 3D structure avoids the use of binder additives and facilitates the release of gas bubbles. The results indicate that the *in situ* formation of nickel sulfides from MOFs through controlled vulcanization can broaden their potential application as efficient bifunctional electrocatalysts for water splitting. The work may provide a novel way to design high-performance MOF catalysts.

Conflicts of interest

There are no conflicts to declare.

Acknowledgements

References

1 J. Yuan, A. Hazarika, Q. Zhao, X. Ling, T. Moot, W. Ma and J. M. Luther, Metal Halide Perovskites in Quantum Dot Solar Cells: Progress and Prospects, *Joule*, 2020, **4**, 1160–1185.

2 F. Zeng, C. Mebrahtu, L. Liao, A. K. Beine and R. Palkovits, Stability and deactivation of OER electrocatalysts: A review, *J. Energy Chem.*, 2022, **69**, 301–329.

3 K. Zhu, X. Zhu and W. Yang, Application of In Situ Techniques for the Characterization of NiFe-Based Oxygen Evolution Reaction (OER) Electrocatalysts, *Angew. Chem., Int. Ed.*, 2019, **58**, 1252–1265.

4 M. Jin, X. Zhang, S. Niu, Q. Wang, R. Huang, R. Ling, J. Huang, R. Shi, A. Amini and C. Cheng, Strategies for Designing High-Performance Hydrogen Evolution Reaction Electrocatalysts at Large Current Densities above 1000 mA cm^{-2}, *ACS Nano*, 2022, **16**, 11577–11597.

5 M. Nath, H. Singh and A. Saxena, Progress of transition metal chalcogenides as efficient electrocatalysts for energy conversion, *Curr. Opin. Electrochem.*, 2022, **34**, 100993.

6 S. N. A. Rahman, M. S. Masdar, M. I. Rosli, E. H. Majlan, T. Husaini, S. K. Kamarudin and W. R. W. Daud, Overview

biohydrogen technologies and application in fuel cell technology, *Renewable Sustainable Energy Rev.*, 2016, **66**, 137–162.

7 T. Wang, H. Xie, M. Chen, A. D'Aloia, J. Cho, G. Wu and Q. Li, Precious metal-free approach to hydrogen electrocatalysis for energy conversion: From mechanism understanding to catalyst design, *Nano Energy*, 2017, **42**, 69–89.

8 D. Zhao, Z. Zhuang, X. Cao, C. Zhang, Q. Peng, C. Chen and Y. Li, Atomic site electrocatalysts for water splitting, oxygen reduction and selective oxidation, *Chem. Soc. Rev.*, 2020, **49**, 2215–2264.

9 C. Zhang, P. Wang, W. Li, Z. Zhang, J. Zhu, Z. Pu, Y. Zhao and S. Mu, MOF-assisted synthesis of octahedral carbon-supported PtCu nanoalloy catalysts for an efficient hydrogen evolution reaction, *J. Mater. Chem. A*, 2020, **8**, 19348–19356.

10 J. Zhu, L. Hu, P. Zhao, L. Y. S. Lee and K.-Y. Wong, Recent Advances in Electrocatalytic Hydrogen Evolution Using Nanoparticles, *Chem. Rev.*, 2020, **120**, 851–918.

11 Z. Chen, K. O. Kirlikovali, P. Li and O. K. Farha, Reticular Chemistry for Highly Porous Metal–Organic Frameworks: The Chemistry and Applications, *Acc. Chem. Res.*, 2022, **55**, 579–591.

12 F.-Y. Yi, R. Zhang, H. Wang, L.-F. Chen, L. Han, H.-L. Jiang and Q. Xu, Metal–Organic Frameworks and Their Composites: Synthesis and Electrochemical Applications, *Small Methods*, 2017, **1**, 1700187.

13 D. Xing, Y. Wang, P. Zhou, Y. Liu, Z. Wang, P. Wang, Z. Zheng, H. Cheng, Y. Dai and B. Huang, Co_3(hexaiminotriphenylene)$_2$: A conductive two-dimensional π–d conjugated metal–organic framework for highly efficient oxygen evolution reaction, *Appl. Catal., B*, 2020, **278**, 119295.

14 X. Z. Song, N. Zhang, X. F. Wang and Z. Tan, Recent advances of metal-organic frameworks and their composites toward oxygen evolution electrocatalysis, *Mater. Today Energy*, 2021, **19**, 100597.

15 J. Li, H. Huang, Y. Li, Y. Tang, D. Mei and C. Zhong, Stable and size-controllable ultrafine Pt nanoparticles derived from a MOF-based single metal ion trap for efficient electrocatalytic hydrogen evolution, *J. Mater. Chem. A*, 2019, **7**, 20239–20246.

16 S. Zheng, X. Guo, H. Xue, K. Pan, C. Liu and H. Pang, Facile one-pot generation of metal oxide/hydroxide@metal–organic framework composites: highly efficient bifunctional electrocatalysts for overall water splitting, *Chem. Commun.*, 2019, **55**, 10904–10907.

17 B. Weng, X. Wang, C. R. Grice, F. Xu and Y. Yan, A new metal–organic open framework enabling facile synthesis of carbon encapsulated transition metal phosphide/sulfide nanoparticle electrocatalysts, *J. Mater. Chem. A*, 2019, **7**, 7168–7178.

18 X. Zhang, H. Pan, Y. Jia, Y. Zhang, Z. Jiang, C. Li, X. Li, L. Bao, R. Ma and K. Wang, Flower-like MOF-74 nanocomposites directed by selenylation towards high-efficient

1302 | *Inorg. Chem. Front.*, 2023, **10**, 1294–1304

This journal is © the Partner Organisations 2023

oxygen evolution, *J. Colloid Interface Sci.*, 2022, **623**, 552–560.

19 F. Yang, P. Zhao, X. Hua, W. Luo, G. Cheng, W. Xing and S. Chen, A cobalt-based hybrid electrocatalyst derived from a carbon nanotube inserted metal–organic framework for efficient water-splitting, *J. Mater. Chem. A*, 2016, **4**, 16057–16063.

20 T. Rodenas, S. Beeg, I. Spanos, S. Neugebauer, F. Girgsdies, G. Algara-Siller, P. P. M. Schleker, P. Jakes, N. Pfänder, M. Willinger, M. Greiner, G. Prieto, R. Schlögl and S. Heumann, 2D Metal Organic Framework-Graphitic Carbon Nanocomposites as Precursors for High-Performance O_2-Evolution Electrocatalysts, *Adv. Energy Mater.*, 2018, **8**, 1802404.

21 Y. Liu, J. Wu, K. P. Hackenberg, J. Zhang, Y. M. Wang, Y. Yang, K. Keyshar, J. Gu, T. Ogitsu, R. Vajtai, J. Lou and P. M. Ajayan, Brandon and B. I. Yakobson, Self-optimizing, highly surface-active layered metal dichalcogenide catalysts for hydrogen evolution, *Nat. Energy*, 2017, **2**, 17127.

22 Y. Guo, T. Park, J. W. Yi, J. Henzie, J. Kim, Z. Wang, B. Jiang, Y. Bando, Y. Sugahara, J. Tang and Y. Yamauchi, Nanoarchitectonics for Transition-Metal-Sulfide-Based Electrocatalysts for Water Splitting, *Adv. Mater.*, 2019, **31**, 1807134.

23 Y. Shi, B. Zhu, X. Guo, W. Li, W. Ma, X. Wu and H. Pang, MOF-derived metal sulfides for electrochemical energy applications, *Energy Storage Mater.*, 2022, **51**, 840–872.

24 M. Fiaz, M. Kashif, M. Fatima, S. R. Batool, M. A. Asghar, M. Shakeel and M. Athar, Synthesis of Efficient TMS@MOF-5 Catalysts for Oxygen Evolution Reaction, *Catal. Lett.*, 2020, **150**, 2648–2659.

25 P. He, Y. Xie, Y. Dou, J. Zhou, A. Zhou, X. Wei and J.-R. Li, Partial Sulfurization of a 2D MOF Array for Highly Efficient Oxygen Evolution Reaction, *ACS Appl. Mater. Interfaces*, 2019, **11**, 41595–41601.

26 D. Gao, W. Zhong, Y. Liu, H. Yu and J. Fan, Synergism of tellurium-rich structure and amorphization of $NiTe_{1+x}$ nanodots for efficient photocatalytic H2-evolution of TiO_2, *Appl. Catal., B*, 2021, **290**, 120057.

27 E. Nurlaela, T. Shinagawa, M. Qureshi, D. S. Dhawale and K. Takanabe, Temperature Dependence of Electrocatalytic and Photocatalytic Oxygen Evolution Reaction Rates Using NiFe Oxide, *ACS Catal.*, 2016, **6**, 1713–1722.

28 H. Chen, Z. Yu, R. Jiang, J. Huang, Y. Hou, Y. Zhang, H. Zhu, B. Wang, M. Wang and W. Tang, Sulfur defect rich Mo-Ni_3S_2 QDs assisted by O-C=O chemical bonding for an efficient electrocatalytic overall water splitting, *Nanoscale*, 2021, **13**, 6644–6653.

29 Y. Liu, X. Zhang, W. Zhang, X. Ge, Y. Wang, X. Zou, X. Zhou and W. Zheng, MXene-Based Quantum Dots Optimize Hydrogen Production via Spontaneous Evolution of Cl- to O-Terminated Surface Groups, *Energy Environ. Mater.*, 2022, e12438, DOI: **10.1002/eem2.12438**.

30 S. Anantharaj, S. R. Ede, K. Karthick, S. Sam Sankar, K. Sangeetha, P. E. Karthik and S. Kundu, Precision and correctness in the evaluation of electrocatalytic water split-ting: revisiting activity parameters with a critical assessment, *Energy Environ. Sci.*, 2018, **11**, 744–771.

31 A. Mesbah, P. Rabu, R. Sibille, S. Lebègue, T. Mazet, B. Malaman and M. François, From Hydrated $Ni_3(OH)_2(C_8H_4O_4)_2(H_2O)_4$ to Anhydrous $Ni_2(OH)_2(C_8H_4O_4)$: Impact of Structural Transformations on Magnetic Properties, *Inorg. Chem.*, 2014, **53**, 872–881.

32 X. Li, X. Shang, Y. Rao, B. Dong, G. Q. Han, W. H. Hu, Y. R. Liu, K. L. Yan, J. Q. Chi, Y. M. Chai and C. G. Liu, Tuning crystal phase of NiS_x through electro-oxidized nickel foam: A novel route for preparing efficient electrocatalysts for oxygen evolution reaction, *Appl. Surf. Sci.*, 2017, **396**, 1034–1043.

33 C. Manjunatha, N. Srinivasa, S. K. Chaitra, M. Sudeep, R. Chandra Kumar and S. Ashoka, Controlled synthesis of nickel sulfide polymorphs: studies on the effect of morphology and crystal structure on OER performance, *Mater. Today Energy*, 2020, **16**, 100414.

34 L. L. Feng, G. Yu, Y. Wu, G. D. Li, H. Li, Y. Sun, T. Asefa, W. Chen and X. Zou, High-Index Faceted Ni_3S_2 Nanosheet Arrays as Highly Active and Ultrastable Electrocatalysts for Water Splitting, *J. Am. Chem. Soc.*, 2015, **137**, 14023–14026.

35 X. Shang, W. H. Hu, G. Q. Han, Z. Z. Liu, B. Dong, Y. R. Liu, X. Li, Y. M. Chai and C. G. Liu, Crystalline phase-function relationship of in situ growth Ni_xS_y controlled by sulfuration degree for oxygen evolution reaction, *Int. J. Hydrogen Energy*, 2016, **41**, 13032–13038.

36 Z. Liu, Y. Qiu, A. Zhang, W. Yang, C. J. Barrow, J. M. Razal and J. Liu, In situ embedding of cobalt sulfide quantum dots among transition metal layered double hydroxides for high performance all-solid-state asymmetric super-capacitors, *J. Mater. Chem. A*, 2021, **9**, 22573–22584.

37 J. Zhou, Z. Han, X. Wang, H. Gai, Z. Chen, T. Guo, X. Hou, L. Xu, X. Hu, M. Huang, S. V. Levchenko and H. Jiang, Discovery of Quantitative Electronic Structure–OER Activity Relationship in Metal–Organic Framework Electrocatalysts Using an Integrated Theoretical–Experimental Approach, *Adv. Funct. Mater.*, 2021, **31**, 2102066.

38 D. Song, H. Guo, K. Huang, H. Zhang, J. Chen, L. Wang, C. Lian and Y. Wang, Carboxylated carbon quantum dot-induced binary metal–organic framework nanosheet synthesis to boost the electrocatalytic performance, *Mater. Today*, 2022, **54**, 42–51.

39 S. Xu, J. Du, J. Li, L. Sun and F. Li, Nickel-selenide templated binary metal–organic frameworks for efficient water oxidation, *J. Mater. Chem. A*, 2020, **8**, 16908–16912.

40 K. Park, J. Kwon, S. Jo, S. Choi, E. Enkhtuvshin, C. Kim, D. Lee, J. Kim, S. Sun, H. Han and T. Song, Simultaneous electrical and defect engineering of nickel iron metal-organic-framework via co-doping of metalloid and non-metal elements for a highly efficient oxygen evolution reaction, *Chem. Eng. J.*, 2022, **439**, 135720.

41 H. Zhao, L. Zhang, L. Dai, F. Yao, Y. Huang, J. Deng, Y. Fu, J. Zhu and J. Sun, Regulating the transformation behavior of nickel iron metal–organic frameworks through a dual-

This journal is © the Partner Organisations 2023

Inorg. Chem. Front., 2023, **10**, 1294–1304 | **1303**

ligand strategy for enhanced oxygen evolution reaction performance, *Appl. Surf. Sci.*, 2022, **592**, 153252.

42 L. Li, C. Sun, B. Shang, Q. Li, J. Lei, N. Li and F. Pan, Tailoring the facets of Ni_3S_2 as a bifunctional electrocatalyst for high-performance overall water-splitting, *J. Mater. Chem. A*, 2019, **7**, 18003–18011.

43 R. Yu, C. Wang, D. Liu, Z. Wu, J. Li and Y. Du, Bimetallic sulfide particles incorporated in Fe/Co-based metal–organic framework ultrathin nanosheets toward boosted electrocatalysis of the oxygen evolution reaction, *Inorg. Chem. Front.*, 2022, **9**, 3130–3137.

44 B. Mohanty, M. Ghorbani-Asl, S. Kretschmer, A. Ghosh, P. Guha, S. K. Panda, B. Jena, A. V. Krasheninnikov and B. K. Jena, MoS_2 Quantum Dots as Efficient Catalyst Materials for the Oxygen Evolution Reaction, *ACS Catal.*, 2018, **8**, 1683–1689.

45 M. Zhao, W. Li, J. Li, W. Hu and C. M. Li, Strong Electronic Interaction Enhanced Electrocatalysis of Metal Sulfide Clusters Embedded Metal–Organic Framework Ultrathin Nanosheets toward Highly Efficient Overall Water Splitting, *Adv. Sci.*, 2020, **7**, 2001965.

46 D. Zhou, S. Wang, Y. Jia, X. Xiong, H. Yang, S. Liu, J. Tang, J. Zhang, D. Liu, L. Zheng, Y. Kuang, X. Sun and B. Liu, NiFe Hydroxide Lattice Tensile Strain: Enhancement of Adsorption of Oxygenated Intermediates for Efficient Water Oxidation Catalysis, *Angew. Chem., Int. Ed.*, 2019, **58**, 736–740.

47 C. F. Li, L. J. Xie, J. W. Zhao, L. F. Gu, H. B. Tang, L. Zheng and G.-R. Li, Interfacial Fe−O−Ni−O−Fe Bonding Regulates the Active Ni Sites of Ni-MOFs via Iron Doping and Decorating with FeOOH for Super-Efficient Oxygen Evolution, *Angew. Chem., Int. Ed.*, 2022, **61**, e202116934.

48 J. W. Zhao, H. Zhang, C. F. Li, X. Zhou, J. Q. Wu, F. Zeng, J. Zhang and G.-R. Li, Key roles of surface Fe sites and Sr vacancies in the perovskite for an efficient oxygen evolution reaction via lattice oxygen oxidation, *Energy Environ. Sci.*, 2022, **15**, 3912–3922.

49 J. W. Zhao, C. F. Li, Z. X. Shi, J. L. Guan and G. R. Li, Boosting Lattice Oxygen Oxidation of Perovskite to Efficiently Catalyze Oxygen Evolution Reaction by FeOOH Decoration, *Research*, 2020, 2020.

50 C. F. Li, T. Y. Shuai, L. R. Zheng, H. B. Tang, J. W. Zhao and G.-R. Li, The key role of carboxylate ligands in Ru@Ni-MOFs/NF in promoting water dissociation kinetics for effective hydrogen evolution in alkaline media, *Chem. Eng. J.*, 2023, **451**, 138618.

51 C. F. Li, L. J. Xie, J. W. Zhao, L. F. Gu, J. Q. Wu and G. R. Li, Interfacial electronic modulation by Fe_2O_3/NiFe-LDHs heterostructures for efficient oxygen evolution at high current density, *Appl. Catal., B*, 2022, **306**, 121097.

52 X. Zheng, X. Han, Y. Zhang, J. Wang, C. Zhong, Y. Deng and W. Hu, Controllable synthesis of nickel sulfide nanocatalysts and their phase-dependent performance for overall water splitting, *Nanoscale*, 2019, **11**, 5646–5654.

53 N. Jiang, Q. Tang, M. Sheng, B. You, D.-E. Jiang and Y. Sun, Nickel sulfides for electrocatalytic hydrogen evolution under alkaline conditions: a case study of crystalline NiS, NiS_2, and Ni_3S_2 nanoparticles, *Catal. Sci. Technol.*, 2016, **6**, 1077–1084.

54 T. Shinagawa, A. T. Garcia-Esparza and K. Takanabe, Insight on Tafel slopes from a microkinetic analysis of aqueous electrocatalysis for energy conversion, *Sci. Rep.*, 2015, **5**, 13801.